J A C S
JOURNAL OF THE AMERICAN CHEMICAL SOCIETY
pubs.acs.org/JACS
Article

The Restoring Force Triangle: A Mnemonic Device for Polymer Mechanochemistry

Yunyan Sun, Fangbai Xie, and Jeffrey S. Moore*

Cite This: https://doi.org/10.1021/jacs.4c10346

Read Online

ACCESS | Metrics & More | Article Recommendations | Supporting Information

ABSTRACT: In polymer mechanochemistry, mechanophores are specific molecular units within the macromolecular backbone that are particularly sensitive to tension. To facilitate understanding of this selective responsiveness, we introduce the restoring force triangle (RFT). The RFT is a mnemonic device intended to provide intuitive insight into how external tensile forces (i.e., stretching) can selectively activate scissile bonds, thereby initiating mechanically driven chemical reactions. The RFT utilizes two easily computable parameters: the effective bond stiffness constant, which measures a bond's resistance to elongation, and the bond dissociation energy, which is the energy required to break a bond. These parameters help categorize reactivity into thermal and mechanical domains, providing a useful framework for developing new mechanophores that are responsive to force but thermally stable. The RFT helps chemists intuitively understand how tensile force contributes to the activation of a putative mechanophore, facilitating the development of mechanochemical reactions and mechano-responsive materials.

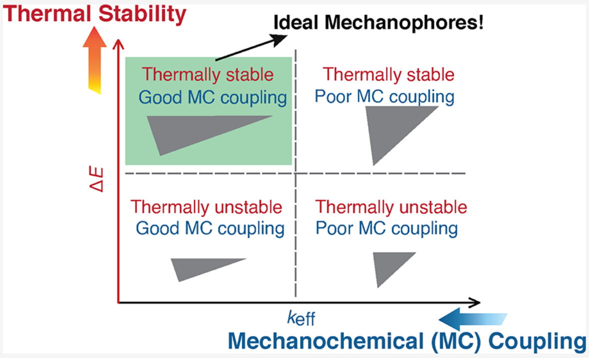

INTRODUCTION

Mechanophores represent a class of molecules that undergo productive covalent bond changes in response to external forces.[1−3] While all bonds are susceptible to force-induced scission, mechanophores are distinctively more susceptible compared to other units in a polymer chain.[4−6] Over the past decade, researchers have synthesized and examined over 100 mechanophores, supporting the hypothesis that specific units undergo selective and productive force-induced covalent bond changes.[1,7,8] Although current computational methods offer precise modeling of these reactivity behaviors,[4,5,9,10] there remains a need for an intuitive approach to understand the selectivity in mechanically driven reactions. This article introduces the restoring force triangle (RFT) as a mnemonic device, designed to enhance our intuitive grasp of mechanophore behavior.

Chemists traditionally analyze reactivity using potential energy and reaction coordinate diagrams. However, here we deviate slightly from this approach to use the RFT to analyze reactivity. Thus, we shift focus to the derivative of potential energy with respect to the reaction coordinate, known as the restoring force plot. Potential energy curves depict the variation in a molecule's internal energy along the reaction coordinate. In contrast, the restoring force plot represents the internal forces a molecule experiences when it is deformed away from its equilibrium structure. This approach naturally provides a means to evaluate the new equilibrium atomic positions of a molecule subjected to external forces. By focusing on the restoring force, we gain a clearer understanding of the directional nature of these forces. Since energy is a scalar quantity and force is a vector, understanding chemical changes driven by an external stretching force applied in a specific direction necessitates considering the force curve, rather than the potential curve, on the reaction coordinate diagram.

The historical foundation of force-reactivity relationships traces back to 1936, when de Boer made a pioneering contribution by theoretically computing a rupture force of 5.6 nN for a canonical carbon−carbon bond, initiating the exploration of mechanical force on bond activation.[11] This exploration was further advanced in 1940 by Kauzmann and Eyring, who estimated the rate of bond rupture under specific tensile forces and proposed the concept of force-modified potential energy surface, thereby emphasizing the importance of mechanical forces in chemical reactions.[12] While these seminal studies, along with many that followed,[5,13−19] focused on bond strength and rupture, there has been a lack of simple models accounting for other molecular aspects, such as the influence of stereochemistry on the selective conversion of external force into chemical activation. The RTF introduced

Received: July 29, 2024
Revised: October 29, 2024
Accepted: October 30, 2024

https://doi.org/10.1021/jacs.4c10346

here aims to construct a mechanical model of mechanophores by identifying key molecular features to address this gap.

Due to the extensive presence of C−C bonds in organic molecules, we present the RFT specifically for mechanophores where the force-induced reactivity stems from tension in C−C bonds. Despite the C−C bond being recognized as strong and prevalent in organic chemistry, many mechanophores activate these bonds to initiate selective bond scission, triggering their mechanochemical transformations.[20−50] Figure 1 illustrates representative examples of mechanophores involving C−C bond scission. Notably, despite the diversity of structure types, they are presumed to share C−C bond scission as the rate-determining step (RDS). While our examination of the RFT has been limited to tensioned C−C bond activations, we anticipate that the principles outlined here will extend to various other bonds and mechanisms beyond homolytic cleavage.

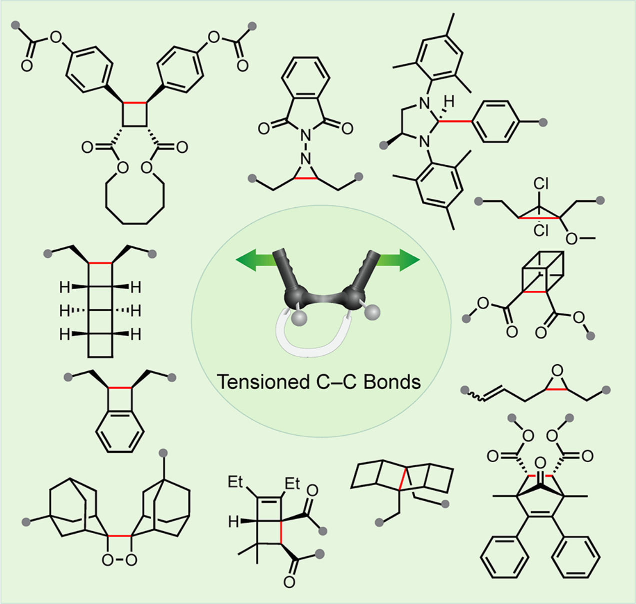

Figure 1. Chemical structures of mechanophores based on C−C bond activations. The bonds highlighted in red are selectively cleaved under tension to initiate specific chemical outcomes. The gray circle represents the atoms to which the force is applied.

Understanding the selectivity in the RDS requires examining the interplay between intrinsic bond energy and mechanochemical coupling, as both thermal activation and mechanical activation contribute to bond cleavage. As discussed in detail below, we construct the RFT by leveraging two molecular features: the effective force constant of the scissile bond (k_{eff}) and the force-free reaction energy (ΔE), which roughly represent the mechanical and thermal components, respectively.

RESULTS AND DISCUSSION

Conceptualization of the RFT. The RFT is based on classical mechanics, specifically in the branch known as statics. This approach does not consider the movement of atoms. Instead, statics focuses on the analysis of force and torque acting on physical systems that do not experience acceleration ($a = 0$) and are in static equilibrium with their environment. When the summation of all forces totals to zero, a mechanical system is said to be in static equilibrium. For a molecular system in static equilibrium, the molecule's internal forces and those applied to the molecule from the environment sum to zero.

In contrast to statics, dynamics is the branch of classical mechanics that studies forces and their effects on motion. Dynamics is also important in mechanochemistry.[9,23,51] However, there is much to be gained by first understanding the static description of bond distortion and scission. This static perspective provides a basis for analyzing how forces act on bonds without the complication of movement, setting the stage for more complex dynamic considerations.[52]

The static description may seem overly simplistic, but it is important to remember that transition state theory (TST) is a static description of reactivity.[53] TST does not explicitly consider the molecular dynamics or the actual motion of the atoms during the reaction. It treats the transition state as a stationary point on the potential energy surface, without accounting for the dynamic nature of molecular motion or the effects of quantum mechanics. Therefore, TST provides a simplified, conceptual framework for understanding reaction rates under force based on the static properties of the transition state.[54]

In developing the RFT, we first explore the simple Hookean spring as a model of the chemical bond. Consider a simple Hookean spring attached at one end to a fixed object. Its equilibrium, "force-free" length equals L_0 (Figure 2a), and k_0, the spring's stiffness constant, is a parameter that describes resistance to deformation. Importantly, the greater k_0, the more resistant the spring is to deform. Note that we use the term "force-free" to indicate the absence of a force, f_a, applied from the environment. It is important to recognize that in the absence of f_a, the spring may still experience an internal restoring force that depends on its displacement. By analogy, a deformed bond will experience a restoring force that depends on its displacement from the equilibrium bond length.

A spring that is stretched to X_1 ($X_1 > L_0$) by an applied force results in mechanical work, correspondingly, the spring's internal energy rises by an amount equal to this work. By analogy, a bond's internal energy rises when it is deformed. To maintain the spring (or bond) in an extended state, the applied force must remain constant. A new equilibrium exists as long as the force remains. However, the instant that the force is released (Figure 2b), the spring is no longer at equilibrium. The spring's internal restoring force, f_r, returns it to the original force-free position. Hooke's law describes how the spring's internal force (i.e., the restoring force) changes with position $\Delta f_r = -k_0\cdot\Delta X$ ($\Delta X = X_1 - L_0$). Using this relationship we can construct the restoring force plot, f_r vs X (Figure 2c). Furthermore, the sign of f_r is opposite in sign to the applied force, f_a, the force that causes stretching.

The incremental work, ΔW, performed on the spring is precisely offset by the change in the spring's internal energy = $-\Delta E$. This gives the relationship $\mathrm{d}W = -\mathrm{d}E = f_r\cdot\mathrm{d}X$ for which $f_r = -k_0\cdot X$ as noted above. The definite integral of this equation from the limits $X = X_1$ to $X = L_0 = 0$ gives the familiar parabolic, force-free potential energy surface (FFPES) along the X coordinate (Figure 2c). Notice that the restoring force plot and force-free potential energy share a derivative-integral relationship. The corresponding energy stored in the spring upon deformation from $X = L_0 = 0$ to $X = X_1$ is represented by the yellow triangle area in the restoring force plot (Figure 2c). To represent a bond, center of mass coordinates using $X = L_0$

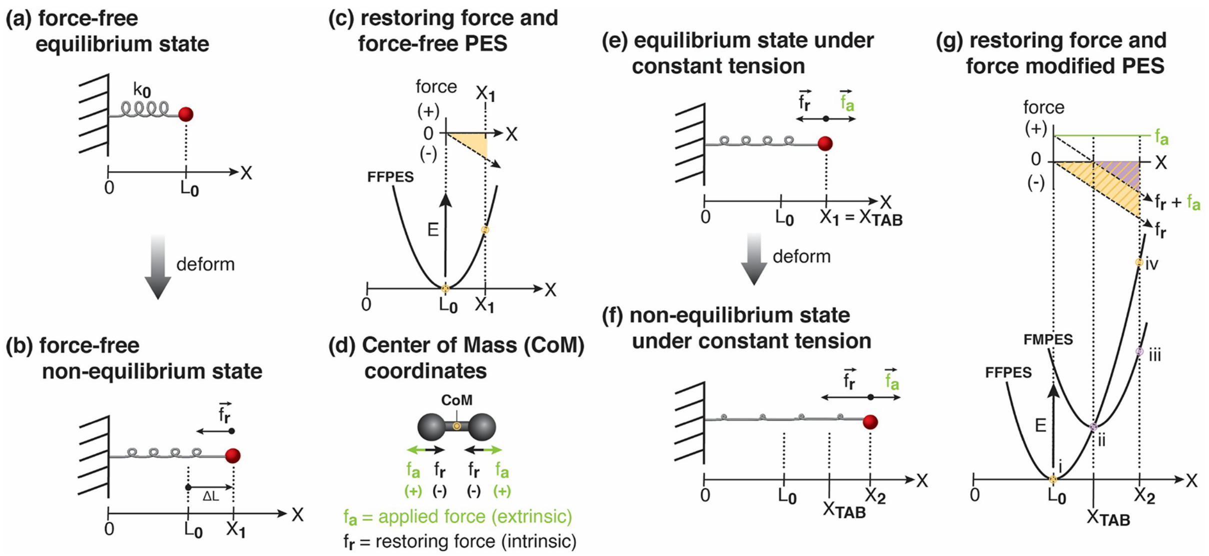

Figure 2. Hookean spring as a simplified model for chemical bond under tension. This set of plots and schematic diagrams illustrate the formalisms and the sign conventions used in this paper, where f_a points in the positive X direction and f_r points in the negative X direction. For center of mass coordinates, positive f_a points away from the center, and positive f_r points toward the center. The derivative-integral relationship $dE/dL = -f_a$ is visualized in these plots. Notably, states of force balance correspond to minima and maxima on the potential energy plot. (a) An equilibrated Hookean spring under force-free condition. (b) An elongated Hookean spring with a displacement of X_1 without any external force. (c) The restoring force plot and the corresponding potential energy surface of a Hookean spring without external force. (d) Center of mass coordinates for describing for the spring. (e) An equilibrated Hookean spring under external force f_a. (f) An elongated Hookean spring with a displacement of X_1 under f_a (where $|f_r| > |f_a|$) (g) The restoring force plot and the corresponding potential energy surface of a Hookean spring under f_a.

= 0 as the point of equilibrium (Figure 2d) are most convenient.

Now consider the case where the same Hookean spring experiences a *permanently* applied constant force, f_a. In the new equilibrium state, the spring will elongate until the restoring force, f_r, equals f_a. We define this new equilibrium state as the tension-activated bond (TAB) and the corresponding displacement as X_{TAB} (Figure 2e). Applying an even greater force will elongate the spring to $X = X_2$ (where $X_2 > X_{TAB}$). Releasing the extra force while maintaining the permanently applied constant force f_a, the spring tends to rebound back to X_{TAB} since $f_r = -k_0 \cdot X_2$ exceeds f_a (Figure 2f).

We can also analyze this process in reference to the potential energy and the restoring force plot, as shown in Figure 2g. When a constant f_a is applied to the spring, the new ground (equilibrium) state shifts to $X = X_{TAB}$, while the spring force constant k_0 remains unchanged. Therefore, a new potential energy surface emerges. This new surface is known as the force-modified potential energy surface (FMPES).[12] The vertex (i.e., local minimum) of the FMPES migrates along the force-free PES (FFPES) to $X = X_{TAB}$, while the shape of the curve remains the same. The restoring force curve of the FMPES is obtained by vertically translating the original plot by f_a. Notably, in the new restoring force curve, X_{TAB} denotes the displacement where the forces balance (i.e., the forces sum to zero).

As f_a increases, the TAB shifts further along the coordinate, leading to a larger value of X_{TAB}. Moreover, the external energy needed from X_{TAB} to X_2 (i.e., ΔE between purple points ii and iii in FMPES) is represented by the purple triangle, and the stored energy from L_0 to X_2 (i.e., ΔE between the yellow points i and iv in FFPES) is represented by the larger yellow triangle (Figure 2g, top).

Construction of the RFT. The Hookean spring model is inadequate for mechanochemistry because it does not predict bond scission. With each increment of applied force, a new ground state is realized, signified by the shifting position of force balance (X-axis intercept of the red dashed line, Figure 3a) and the corresponding shift in the minimum of the force-modified potential energy surface (FMPES) (blue dashed

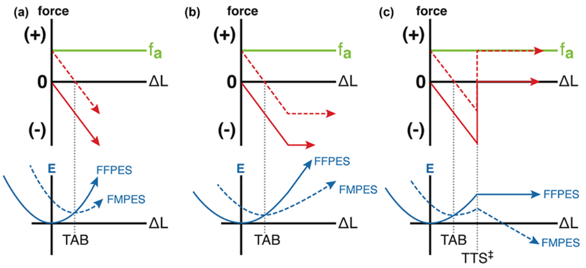

Figure 3. Force profiles for mechanical systems with various restoring force characteristics. This figure illustrates the force profiles of mechanical systems with different restoring force characteristics, depicted both in the absence (solid lines) and presence (dashed lines) of applied tensional force (f_a = horizontal green line). The solid red line represents the restoring force versus displacement with no applied force, while the red dashed lines show the sum of the restoring force and a constant applied force. Each X-intercept represents a state of force balance where $f_r = -f_a$. The blue plots indicate the corresponding internal energies without (solid = force-free potential energy surface, FFPES) and with (dashed = force-modified potential energy surface, FMPES) an applied field. Notice the derivative-integral relationship between force and energy ($f = -dE/dl$). In particular, wherever the force plots intercept the X-axis, it leads to a minimum or maximum in the energy plot. These points of force balance are identified as follows: TAB = tension-activated bond, TTS‡ = tensioned transition state. (a) The Hookean spring model. (b) A spring that initially follows Hookean behavior but then exhibits a constant restoring force after a certain displacement. (c) A Hookean spring that suddenly breaks upon over stretching.

https://doi.org/10.1021/jacs.4c10346

curve, Figure 3a). The derivative-integral relationship between the blue and red curves is evident. As the applied force increases, the energy value associated with each new minimum rises; there is no point at which the force diminishes and the energy falls. This behavior contrasts with that of a chemical bond, where the atoms ultimately dissociate. In a chemical bond, the restoring force weakens with increasing stretch as an energy barrier is surmounted, leading to bond dissociation.

We began to explore scenarios where the restoring force deviates from classical Hooke's law, specifically cases involving more complex anharmonic potential energy wells. Consider a spring where the restoring force first increases linearly with extension and then reaches a plateau (Figure 3b). The restoring force exhibits a nonlinear response to the spring's extension. The corresponding force-free potential energy surface (FFPES) is anharmonic. It initially follows a parabolic curve but, upon reaching the extension point where the force plateau begins, the FFPES rises linearly. When a constant f_a is applied, the sum of forces ($f_a + f_r$) results in a force vs extension function that is vertically shifted from the original f_r plot (dashed red line segments in Figure 3b. The minimum of the force-modified potential energy surface (FMPES) shifts (i.e., TAB) to the point where the forces balance (dashed blue curve in Figure 3b). The slope of the FMPES increases until the plateau point, beyond which it rises with a constant slope. Notice that due to the displacement of the total force curve, after the plateau point, the slope of the FMPES is smaller than the slope of the FFPES.

Another intriguing scenario involves a Hookean spring that suddenly breaks upon overstretching. In this case, the restoring force initially behaves as a linear function of displacement but abruptly drops to zero at the breaking point (Figure 3c, top, red solid line). The corresponding force-free potential energy surface (FFPES) initially follows a parabolic curve before plateauing (Figure 3c, bottom, blue solid line). When a constant force f_a is applied to the system, the plot representing the sum of forces shifts upward and becomes positive after the point of bond scission (Figure 3c, top, red dashed line). Consequently, the force-modified potential energy surface (FMPES) starts to decrease linearly beyond the bond scission point, creating a local maximum. We define this local maximum as the tensioned transition state (TTS‡), analogous to the transition state on a reaction coordinate diagram for a chemical reaction. Interestingly, if we gradually increase the value of f_a (below the bond scission force), the location of the tension-activated bond (TAB) shifts to the right, while the location of the TTS‡ remains unchanged. This indicates that the position of the TTS‡ on the reaction coordinate does not depend on f_a, highlighting an important limitation of this model (Figure S1). Overall, we conclude that while an anharmonic potential energy well is necessary, it is not sufficient to generate a TTS‡ (Figure 3b). For a TTS‡ to form, the restoring force must reestablish force balance at some point, as illustrated in Figure 3c, to generate a local maximum. Hence, there is a need to further refine our analysis of the restoring force profile.

For actual bond cleavages under tension, a discontinuous change in f_r versus extension seems unlikely (Figure 3c). While such an abrupt change might be expected for a mechanical object that catastrophically fails, a pair of interacting atoms are likely to have gradually diminishing bonding forces as they are stretched. Therefore, in the case of a chemical bond, we would expect f_r to initially increase, reach a maximum value, and then gradually decrease until it eventually reaches zero. To intuitively understand these linear and nonlinear force responses, imagine yourself drawing various archery bows. As shown in Figure 4a, the restoring force curve of a simple recurve bow resembles a Hookean spring, with f_r increasing roughly linearly with draw distance. Intriguingly, for compound bows, due to their pulley/cam design (Figure 4b), the restoring force curve increases at first but then starts to decrease as it is pulled toward full draw.[55,56] This "let-off" (Figure 4a) makes it easier to hold the bow near full draw while maintaining a large potential energy, which translates to high arrow velocity. The exact curve varies in different kinds of compound bows (Figure 4a). The curve with long plateau in the cam wheel compound bow seems less likely for molecules. Notably, the shape of the restoring force curve for the round wheel compound bow can be approximated by a symmetrical triangle.

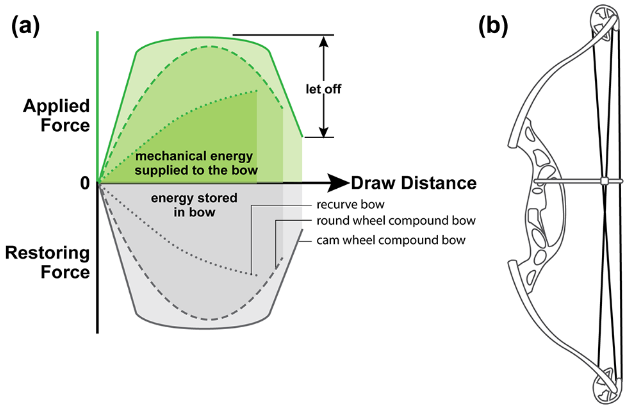

Figure 4. Various archery bows and their corresponding restoring force curves. Notice that the round wheel compound bow exhibits a restoring force profile that approximates a triangular shape. (a)The applied and restoring force curves of recurve bow and compound bow. (b)The mechanical design of a typical compound bow.

Reasoning by analogy to the restoring force profile of the compound bow, we envisioned that a triangular shape could approximate the key features of the restoring force for the C—C bond. This analogy motivated us to introduce a mnemonic device called the Restoring Force Triangle (RFT). When a C—C bond is subjected to tension, it transitions through several states: starting from the force-free ground state (GS), moving to the new stretched equilibrium state (i.e., the tension-activated bond or TAB), then to the tensioned transition state (TTS‡), and, upon surpassing the barrier at the TTS‡, reaching the cleaved tensioned intermediate (TI) (Figure 5a). These states emerge from a restoring force profile that resembles a symmetrical triangle, with edges defined by a linear Hookean region, followed by a linear let-off to zero (Figure 5b, top, red solid line). The third edge of the triangle is the *X*-axis where $f = 0$. The corresponding force-free potential energy surface (FFPES) of this RFT is shown in Figure 5b, bottom. It has an anharmonic potential, and the area of the RFT approximates the bond dissociation energy.

Upon the application of a constant f_a, the RFT shifts upward. The sloped edges of the triangle now reflect the sum of $f_r + f_a$, while the horizontal edge represents the constant f_a. The two *X*-axis intercepts of the force-shifted RFT define the positions of the local minimum TAB and the local maximum TTS‡ in the force-modified potential energy surface (FMPES), respectively (Figure 5b, bottom). The RFT need not be

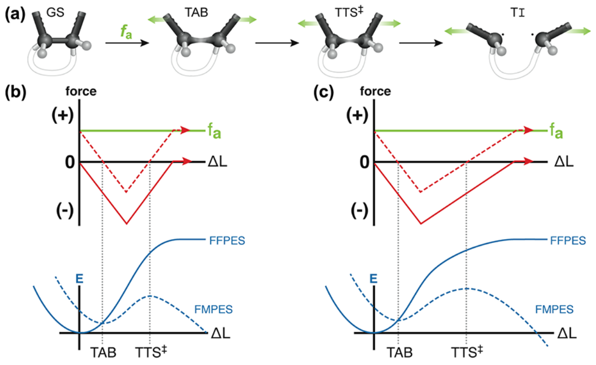

Figure 5. New states emerge upon mechanical activation. (a) Four stages in tension activated C−C bond. (b) Symmetric RTF. (c) Asymmetric RTF with a less steep back slope.

symmetrical. For example, asymmetry occurs when the slopes of the RFT edges differ, such as in the case of a gradual let-off (i.e., a less steep back slope) (Figure 5c, top). Since the front slope is unchanged, the location of the tension-activated bond (TAB) remains the same, whereas the gradual let-off shifts the tensioned transition state ($\mathrm{TTS}^{\ddagger}$) further to the right.

By gradually increasing the complexity of the restoring force curve from the simple linear model of a Hookean spring to the RFT inspired by the compound bow, we have obtained relatively accurate potential energy curves that resemble some classical intermolecular potential energy diagrams (e.g., Morse potential and Lennard-Jones potential). This progress motivates us to revisit the original mechanochemistry model developed by Kauzmann and Eyring in 1940,[12] which is based on the Morse potential.

The Morse function describes the potential of diatomic molecules with an equilibrium bond length L_0 and bond dissociation energy U_0 (Figure 6a).[57,58] The derivative of the Morse function with respect to interatomic displacement yields the restoring force curve, which describes how strongly the pair of atoms resist being displaced from equilibrium. The slope of the restoring force curve at L_0 is the Hookean force constant, k, which characterizes the bond's stiffness or resistance to deformation. The maximum value of the force curve corresponds to f_{max}, and the area under the force curve corresponds to U_0.

We can use features of the Morse restoring force curve to parametrize the Restoring Force Triangle (RFT) mnemonic (Figure 6a). The RFT's area is approximately U_0, its front slope is $-k$, and its back slope, $k/8$, takes on the value of the slope of the Morse function's restoring force curve at its inflection point.[59] This parametrization is reasonable given that the RFT mnemonic is an approximation of the Morse restoring force curve. This approximation is arbitrary and not quantitatively oriented, but rather, it is intended to provide intuitive insights into the reactivity of tensioned bonds. Although the Morse function is originally proposed for diatomic molecules, it serves as a reasonable approximation for more complex bonds, such as C−C bonds in polyatomic molecules.

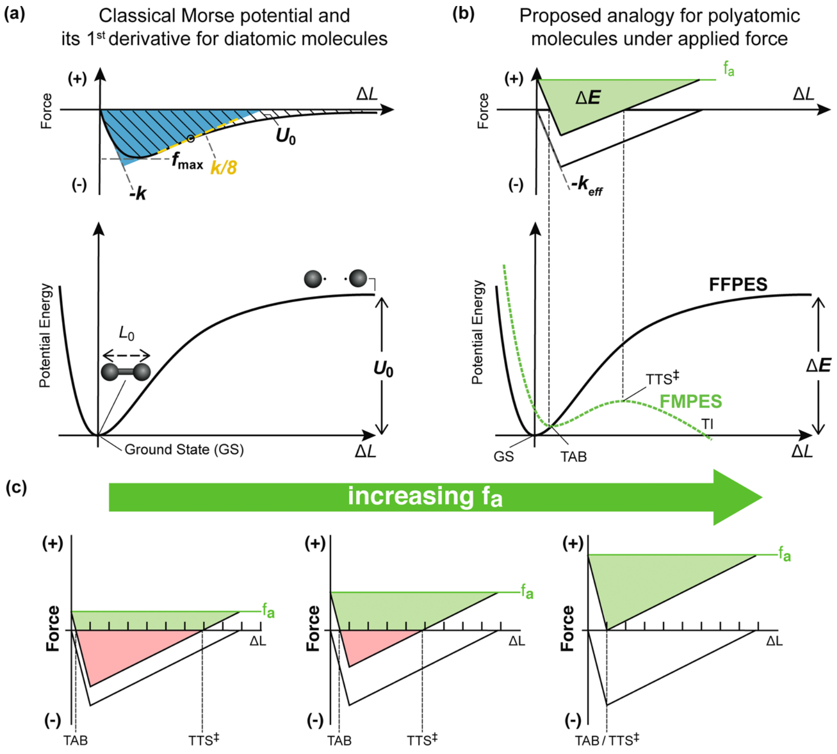

Figure 6. Morse potential and its restoring force curve, and the RFT under applied force. (a) The classical Morse potential (bottom) and its restoring force curve (top) for diatomic molecules. The blue shaded region represents the RFT for the Morse restoring force curve. (b) The proposed analogy for polyatomic systems. When extrapolating the Morse function to polyatomic molecules, U_0 is replaced with ΔE, and k is replaced with keff. Here, ΔE is the force-free bond dissociation energy, and k_{eff} is the stiffness constant that embodies the bond's stereochemical, geometrical and electronic features that transmit the tensile force to the stretching bond. (c) The RFT under the influence of increasing f_a. The total area of the RFT equals the force-free bond dissociation energy, ΔE. This total energy is subdivided into contributions supplied by mechanical work (green) and thermal energy (red).

To translate the classic Morse potential to polyatomic molecules, we propose an analogy with modified key parameters in the curve (Figure 6b). Specifically, U_0 is replaced with ΔE (force-free bond dissociation energy), and k is replaced with k_{eff} (effective Hookean force constant). While the ΔE in polyatomics closely maps to the diatomic U_0, it is instructive to consider the meaning of the force constant, which has a somewhat more complicated mapping. In diatomic molecules, stretching is assumed to occur along the bond axis. For a C−C bond in polyatomics, however, the pulling force is transmitted through the substituents (i.e., handles) attached to the carbon atoms, which are arranged in approximately tetrahedral geometry. The ability of these substituents to transmit force to the bond depends on stereochemical,[43,60] geometrical (e.g., rigid lever arms),[41,61,62] and electronic features.[22,63,64] We therefore hypothesized that this more complex force transmission is captured by the effective Hookean constant k_{eff}, which represents the resistance of the scissile bond toward remotely applied force from the handle. We note that, as suggested by our previous work, mechanophores have roughly constant k_{eff} values near the GS.[59] This simplification aligns with the idea that the bond's stiffness constant reflects its resistance to stretching deformation under tension.

By applying the RFT mnemonic, we can predict the positions of the TAB and the TTS‡ as a function of the applied force (Figure 6b,c). As f_a increases, the RFT shifts vertically because it reflects the sum of $f_r + f_a$. This vertical shift causes the X-axis intercepts to move to new positions along the reaction coordinate. Specifically, the TAB shifts toward the tensioned intermediate (TI), indicating an increasingly destabilized ground state under force. In contrast, the TTS‡ is reached at earlier stages with each increase in f_a, aligning intuitively with the Hammond postulate.[65] Intriguingly, when f_a increases to the point where $f_a = f_{\max}$, the TAB and TTS‡ converge to a single geometry, suggesting a barrierless reaction process (Figure 6c). Although challenging to depict using the RFT, a further increase in f_a (i.e., $f_a > f_{\max}$) will also result in a barrierless bond cleavage process. These straightforward deductions from the RFT align well with high-level simulation results previously reported for several mechanophore systems.[9,10,29,64]

In addition to pinpointing the positions of the TAB and TTS‡ on the reaction coordinate, the RFT helps to assign the energetic contributions to bond scission. The energy needed to dissociate a C−C bond under tension combines both mechanical and thermal contributions. The RFT allows us to partition these relative contributions as a function of the applied force. As force is applied and the RFT rises above the X-axis, mechanical work drives bond scission, represented by the area of the RFT above the $X = 0$ axis (shaded green in Figure 6c). The portion of the RFT below the X-axis represents the energy that must be supplied through thermal activation (colored red in Figure 6c). It is evident that the contribution of thermal energy required for bond scission decreases and eventually vanishes with increasing f_a.[16]

A deeper analysis can be achieved by segmenting the RFT according to the states encountered during bond extension. A tensile force extends the ground state (GS) to the new equilibrium state TAB (Figure 7a), destabilizing the bond by an amount $\Delta E_{\text{GS-distort}}$, represented by area A on the RFT (blue triangle in Figure 7b). As the bond progresses from ΔL_{TAB} to $\Delta L_{\text{TTS}\ddagger}$, mechanical work supplied through f_a contributes energy to bond scission, ΔE_{force}, corresponding to the rectangular area B in Figure 7b and equivalent to $f_a \bullet (\Delta L_{\text{TTS}\ddagger} - \Delta L_{\text{TAB}})$. For applied forces less than $f_{\max}$, a thermal activation barrier remains. The height of this barrier, $\Delta E^\ddagger$, is represented by the area of the RFT below the X-axis.[6,16] The area C represents the internal energy difference between TTS‡ and ruptured bond. Beyond the TTS‡, additional mechanical work is imparted to the bond up to the point of scission, equating to another rectangular (area $C + D$). This additional mechanical energy given to the bond post TTS‡ is represented by area D and may contribute to dynamical effects, leading to reaction trajectories that diverge from the statistical outcomes predicted by conventional transition state theory.[23,51] Recall from Figure 6 that the total area of the RFT equals the force-free bond dissociation energy, ΔE. Therefore, the thermal activation barrier is equal to the difference between ΔE and the contributions of mechanical work imparted to the bond during the various stages of the reaction ($\Delta E^\ddagger = \Delta E - A - B - C$) as shown in Figure 7. The shape and area of the RFT are determined entirely by the effective stiffness k_{eff} and bond dissociation energy ΔE. Using these parameters and the applied force f_a, we can calculate the positions of the TAB and the TTS, as well as the areas of the subregions within the RFT. Detailed results, including derivations, are provided in the Supporting Information. Additionally, we have developed an interactive Python-based tool that allows users to input parameters and visualize the RFT and associated energy

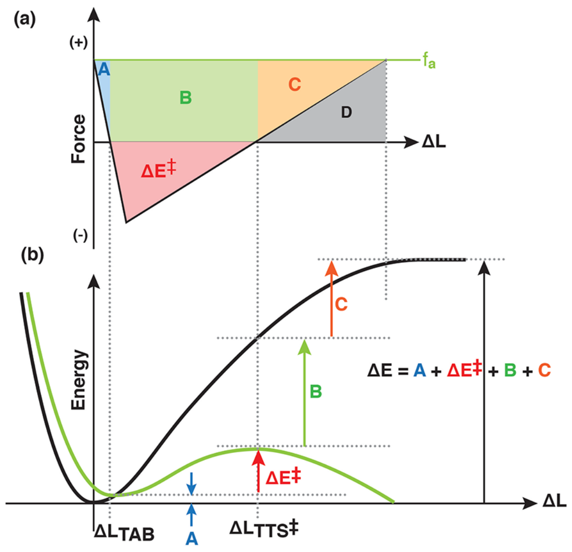

Figure 7. Segmentation of the energy contributions to bond scission. (a) The total area of the RFT represents the force-free bond dissociation energy, ΔE. The RFT is subdivided vertically into mechanical work (above the X-axis) and thermal energy (below the X-axis). Horizontal segmentation corresponds to the mechanical work imparted to distort the ground state to the TAB (area A), the mechanical work progressing from the TAB to the TTS‡ (area B), the internal energy needed to reach bond scission post-TTS‡ (area C), and the external mechanical energy post-TTS‡ (area D). Mechanical work lowers the barrier for bond dissociation, which is surmounted by thermal activation energy ($\Delta E^\ddagger$). (b) The force-free potential energy (black curve) and force-modified potential energy (green curve), labeled with the corresponding energies indicated in the RFT. The total energy in for dissociation is the sum of the segmented areas. See Supporting Information for quantitative derivations of each area.

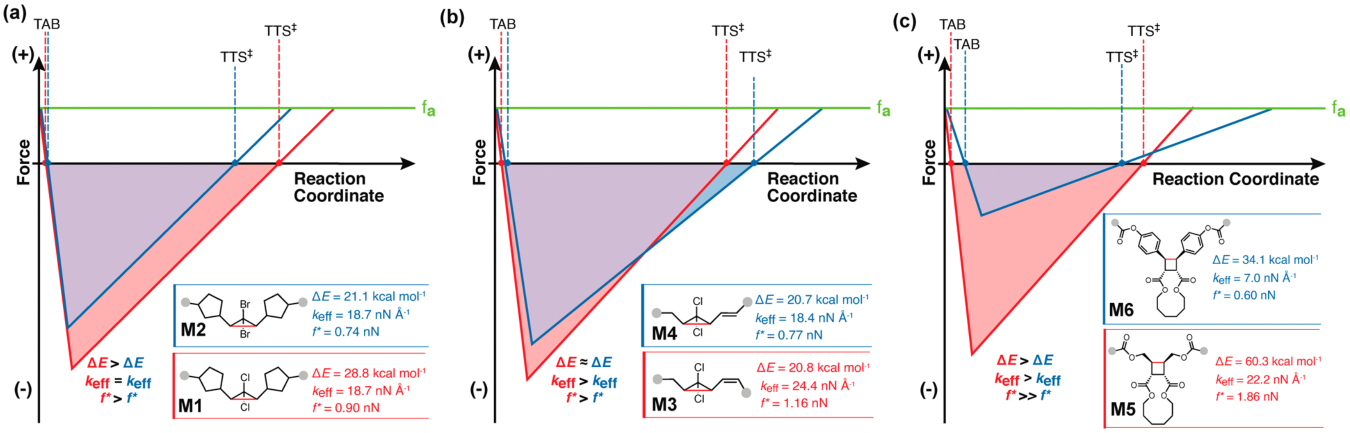

Figure 8. Comparative analyses using the RFT mnemonic. After computing ΔE and k_{eff}, the RFTs for each mechanophore are plotted at the same scale. Differences in mechanochemical activity are revealed by comparing the area below the X-axis. The locations of the TAB and the TTS‡ are indicated by the X-axis intercepts. (a) Mechanophores with nearly identical stiffness but different bond energies. (b) Mechanophores with nearly identical bond energies but different bond stiffnesses. (c) Mechanophores that differ in both bond energies and stiffnesses.

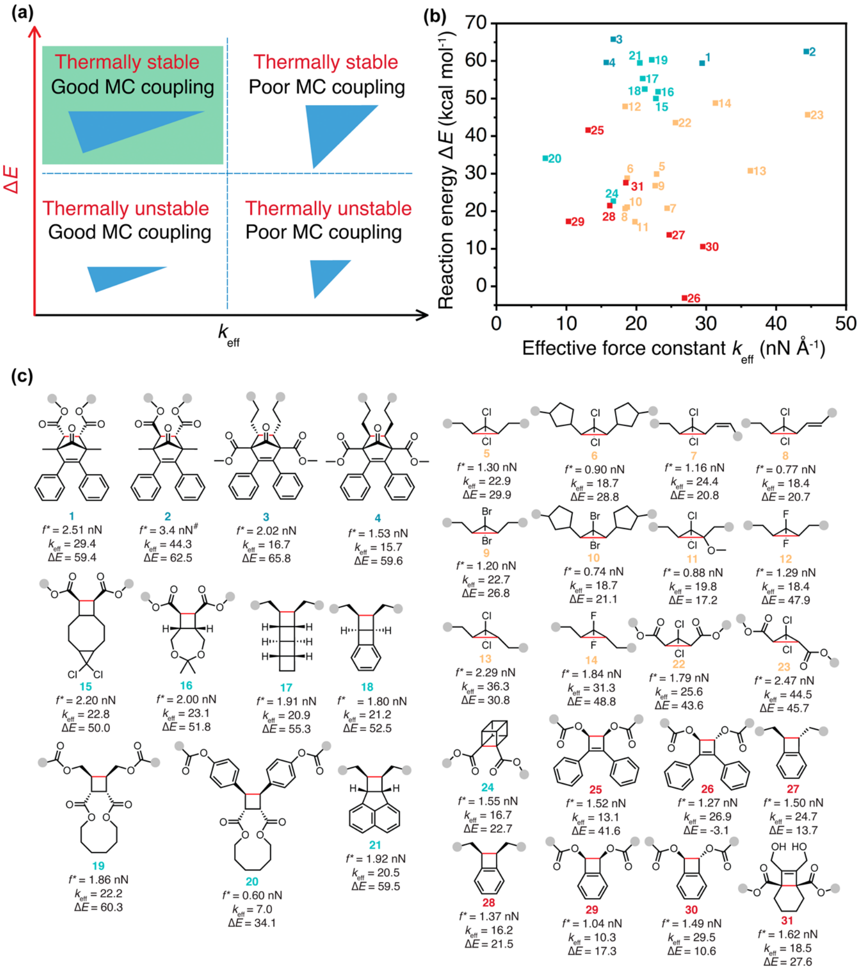

Figure 9. Mechanophore activity matrix (MAX)as a classification tool. (a) Schematic diagram of the MAX, a quad chart for mechanochemistry. (b) Plot of 30 known mechanophores within the MAX framework. Each mechanophore is activated by C−C bond scission, with calculated values of k_{eff} and ΔE, and measured experimental transition force (f^*). The upper left quadrant highlights the privileged mechanophores that are thermally stable but mechanically active, including the prominent NEO mechanophores **3** and **4**, followed by the cyclobutanes. Color coding maps onto the mechanophore scaffold: bicyclic NEO is blue, cyclobutanes are cyan, cyclopropanes are yellow, and benzocyclobutenes are red. (c) Chemical structures and data for the **31** known mechanophores. #: the f^* of **2** is not experimentally determined, so computed f^* was used instead. The gray circle represents the atoms to which the force is applied.

plots, with instructions provided in the Supporting Information.

Application of the RFT. The two key features that emerge from the RFT to describe polyatomic molecules are k_{eff} and

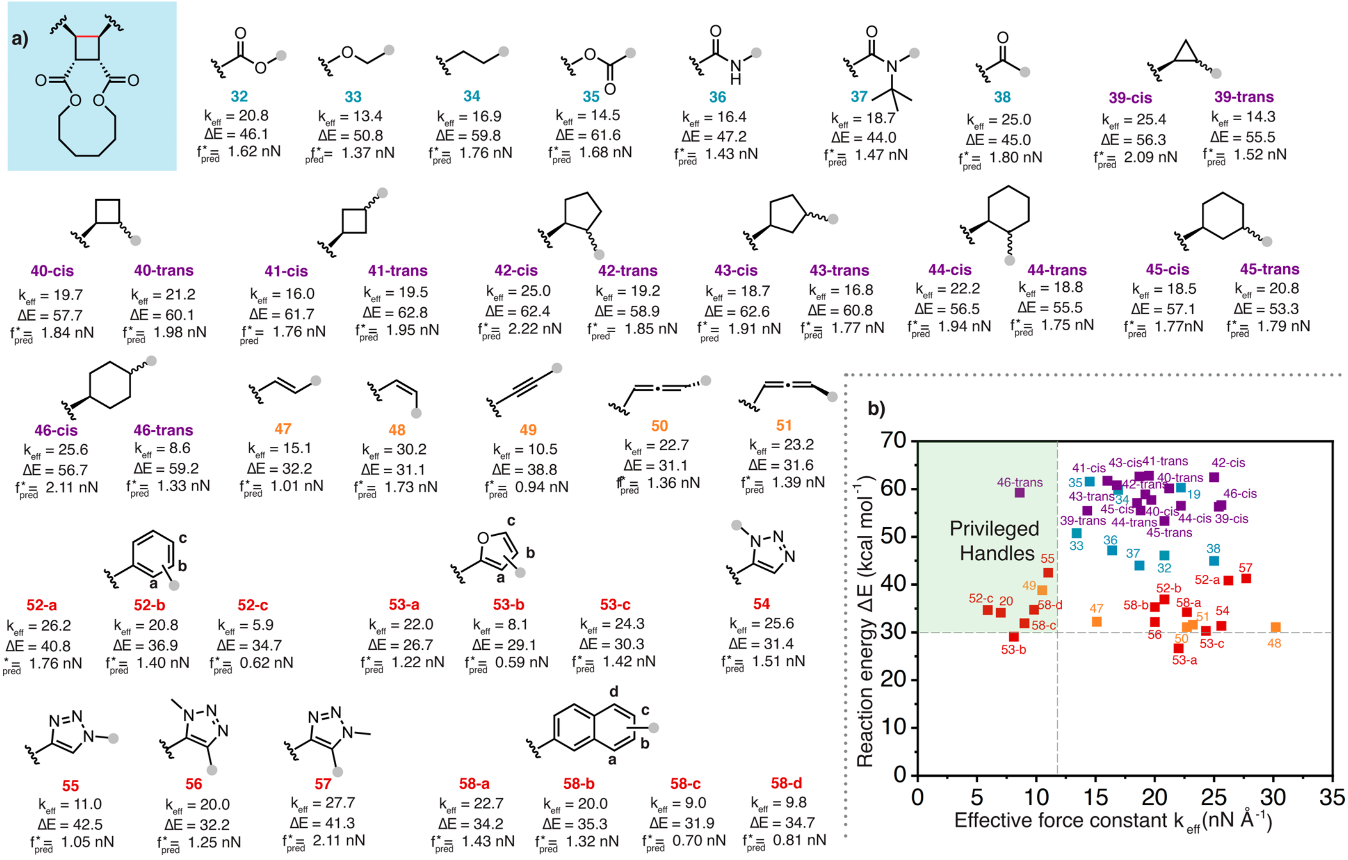

Figure 10. (a) Calculated k_{eff} (nN Å^{-1}), ΔE (kcal mol^{-1}), and predicted transition force ($f^*_{\text{predicted}}$, nN) values of different handles on a representative cyclobutane mechanophore. The gray circle represents the atoms to which the force is applied. Different handle classes are color coded. The $f^*_{\text{predicted}}$ values are calculated using the formula: $f^*_{\text{predicted}} = 0.0238 \times \Delta E + 0.0492 \times k_{\text{eff}} - 0.499$, which was reported in our previously work.[59] (b) Mechanophore activity matrix of the above handles on a cyclobutane mechanophore. The matrix is partitioned into four areas by two dash lines: k_{eff} = 12.0 nN Å^{-1} and ΔE = 30.0 kcal mol^{-1}. Privileged handles that locate on the top left region are highlighted.

ΔE. Both can be easily computed using commonly practiced methods such as Density Functional Theory (DFT). Importantly, these calculations do not require locating the transition-state structures, which can be a tedious task, especially with the added complication of a constant tensile force. Instead, the calculation of k_{eff} typically involves performing simple geometry optimizations at three different values of f_a. We note that k_{eff} represents the overall spring behavior of the specific bond when the mechanophore is subjected to external force through its molecular handles, capturing the stereochemical, regiochemical, and electronic effects as key molecular features. Additionally, the calculation of ΔE is accomplished by two force-free optimizations and two single-point energy simulations, making this method highly suitable for large-scale computational screening in the design of mechanophores. A detailed tutorial for the simulation can be found in our recent report.[59]

To facilitate a comparative analysis of mechanophore activity, we utilize the RFT mnemonic, which can be constructed using computed values of ΔE and k_{eff}. Comparing RFTs visually illustrates the behavior and mechanochemical activity of mechanophores. For example, C−C bonds with lower resistance to deformation (i.e., smaller k_{eff}) or those that are intrinsically more reactive (i.e., smaller ΔE) are expected to display enhanced reactivity under tension. Figure 8 illustrates three such comparisons.

Consider first the gem-dichlorocyclopropane (gDCC) mechanophore **M1** and gem-dibromocyclopropane (gDBC) mechanophore **M2**, both with identical cyclic-alkyl handles (Figure 8a). These mechanophores exhibit the same k_{eff} values while the gDBC shows a lower ΔE value.[59] As a result, two RFTs with identical shapes but distinct areas are obtained. Upon the application of f_a, **M1** and **M2** share an equally deformed TAB, while **M2** exhibits an earlier TTS‡. Importantly, **M2**, with a smaller ΔE value, shows a significantly smaller $\Delta E^{\ddagger}$ value (represented by the purple triangle area in Figure 8a), indicating its enhanced reactivity under force compared to **M1**. These straightforward deductions align well with experimental transition force (f^*) values measured from single-molecule force spectroscopy tests.[41]

In another example, for mechanophores having identical core structures but different handles (i.e., **M3** and **M4** in Figure 8b), we expect two RFTs with the same areas but different shapes. **M4** has a slightly more distorted TAB and a significantly later TTS‡. Therefore, mechanical force tends to contribute more to both $\Delta E_{\text{GS-distort}}$ (area A) and ΔE_{force} (area B) in **M4**, accounting for its lower f^* value (i.e., smaller $\Delta E^{\ddagger}$ or the triangle area under x axis) compared to **M3** (Figure 8b).[61]

We can also consider a more extreme case shown in Figure 8c, where **M6** exhibits significantly smaller values for both k_{eff} and ΔE compared to **M5**. By comparing the two RFTs, a significantly smaller $\Delta E^{\ddagger}$ for **M6** is expected, consistent with the experimental f^* values.[66]

The RFT's key parameters, ΔE and k_{eff}, elucidate a critical insight: reactivity can be distinctly partitioned into thermal and mechanical contributions.[59] This separation fundamentally redefines our approach to mechanophore invention. Traditionally, the prevailing view before the advent of mechanophores was that mechanical activation necessitated designing molecules with weak (i.e., small ΔE) bonds. The rationale was to enhance mechanical reactivity by sacrificing thermal stability. While this concept is sound, it misses the opportunity to view molecular invention through a new lens. By reducing k_{eff}, we can create mechanophores that exhibit significant mechanical reactivity while retaining robust thermal stability (i.e., large ΔE). This paradigm shift allows us to achieve mechanical activation without compromising thermal stability, effectively enabling us to tailor both mechanical and thermal properties in a single molecular framework. We note that since the RFT is approximated from the Morse potential, it is assumed there is no true barrier (i.e., a well-defined transition state) in the force-free state. Therefore, it is important to recognize the limitations of the RFT when applying it for quantitative analysis.

To further conceptualize this paradigm shift, we introduce a visual tool that distills the essence of mechanophore invention into a clear and practical framework. We present the "mechanophore activity matrix" (MAX) in the form of a quad chart, akin to a Punnett square, specifically tailored for mechanochemistry. A schematic diagram is shown in Figure 9a. Unlike a traditional Punnett square, this matrix considers two traits: thermal stability (the rows) classified as low (small ΔE) or high (large ΔE), and effective stiffness (the columns) classified as low (small k_{eff}) or high (large k_{eff}). This creates four distinct mechanophore phenotypes: (i) thermally unstable and mechanochemically active,(ii) thermally unstable and mechanochemically inactive,(iii) thermally stable and mechanochemically active, and (iv) thermally stable and mechanochemically inactive. This matrix is not only practical and simple but also computable, providing a valuable tool for predicting and designing the mechanochemical behavior of various mechanophores.

We put the MAX into action as a powerful classification tool, enabling the identification of molecular features through pattern recognition. Our available data set consists of 31 known mechanophores (Figure 9c), all activated by C−C bond scission, for which k_{eff} and ΔE have been calculated.[59] Additionally, the experimental transition force (f^*) for these mechanophores have been measured. Figure 9b organizes these data according to the matrix arrangement. Structurally similar mechanophores are expected to cluster provided they react by similar mechanisms. Outliers flag the possibility of mechanistic deviation. The privileged mechanophores—thermally stable but mechanically active—reside in the upper left quadrant. Among these, the norborn-2-en-7-one (**NEO**) mechanophores **3** and **4** prominently emerge,[59] with the family of cyclobutanes following closely. Cubane mechanophore (**24**) appears as an outlier to the cyclobutane family and may react by an alternative mechanism.[33] Lever arms from *p*-arene rings notably enhance mechanochemical activity, as seen with mechanophore **20**.[62] Stereochemistry also plays a crucial role, illustrated by the differences between mechanophores **1**, **2**, **3**, and **4**.[59] By populating this matrix with bonds and atoms, we can now predict new reactivity and cast emerging and future mechanophores into a comparable light. This tool not only aids in the identification of promising mechanophores but also frames our understanding in a way that could lead to groundbreaking discoveries in mechanochemistry, pushing the boundaries of what is possible in the field.

We envision the MAX can also be utilized to identify the privileged handles that result small k_{eff} but reasonably high ΔE values to maximize mechanochemical coupling while maintaining the thermal stability of mechanophores. We chose cyclobutane as one of the most widely used and thermally stable mechanophores (Figure 10a) as the example.[22,27−29,34,44,45] Over 40 synthetically relevant handles were examined by calculating their k_{eff} and ΔE values, encompassing common linear handles (blue color), cyclic aliphatic handles that are known to have lever-arm effects (purple color),[41] alkenyl and alkynyl handles (orange color), and arenyl-like rigid ring handles (red color). We also employed the linear regression tool developed in our previous work to predict the transition force ($f^*_{\mathrm{predicted}}$) in the kinetic region of typically single molecule force spectroscopy tests.[59]

Among the common linear handles, the ether handle **33** and the ester handle **35** exhibit fairly good mechanochemical coupling with k_{eff} values of 13.4 and 14.5 nN Å^{-1}, respectively. Compared to a typical amide handle **36**, the *t*-Bu substituted tertiary amide handle **37** slightly weakens the scissile C−C bond but is predicted to have a larger k_{eff} value of 18.7 nN Å^{-1}, giving a comparable $f^*_{\mathrm{predicted}}$ of 1.47 nN. For cyclic aliphatic handles, we examined 3 to 6 membered rings. Intriguingly, the stereo- and regio-chemistry of the ring are predicted to play an important role on the k_{eff} values. The handle **46-trans** exhibits an exceptionally small k_{eff} of 8.6 nN Å^{-1}. As shown in Figure S25, the methyl substituent and the cyclobutane core are both locked in the equatorial position in the chair conformation of **46-trans** under tensile force. This almost parallel alignment likely contributes to the enhanced mechanochemical coupling in **46-trans**. The *E*-alkenyl handle **47** gives an almost identical ΔE value compared to *Z*-alkenyl handle **48**, while showing a significantly smaller k_{eff}. The improved mechanochemical coupling predicted for the *E*-olefin is consistent with reported lever arm effects.[61] The rigid alkynyl handle **49** exhibits a slightly higher ΔE compared to alkenyl handles but shows a surprisingly low k_{eff}, implying its great potential as a synthetically straightforward moiety to promote mechanochemical coupling. Allenyl motifs recently attracted attention as novel functional groups in polymer main chains; we therefore also evaluated their performances as handles in mechanochemistry.[67,68] Only moderate ΔE and k_{eff} values were observed in two different stereoisomers **50** and **51**, giving a $f^*_{\mathrm{predicted}}$ of ∼1.4 nN. We also tested the phenyl handle **52** as a known moiety to promote the reactivity under tension.[66] Consistent with a recently reported work, the para-regioisomer (**52-c**) shows the most pronounced mechanochemical coupling, giving a low k_{eff} of 5.9 nN Å^{-1}.[62] Attracted by the superior behavior of phenyl handles, we are curious to examine furan and triazole handles, as these motifs have been extensively used in dynamic covalent chemistry and click chemistry, respectively.[69,70] Similar to **52**, comparable ΔE but distinct k_{eff} values were observed in different furan regioisomers. A fairly small k_{eff} of 8.1 nN Å^{-1} was calculated in **53-b**, giving a $f^*_{\mathrm{predicted}}$ of ∼0.59 nN. The 1,4-triazole (**55**) exhibited a notably smaller k_{eff} of 11.0 nN Å^{-1} but a slightly higher ΔE of 42.5 kcal mol^{-1} compared to the 1,5-isomer **54**, resulting in $f^*_{\mathrm{predicted}}$ of ∼1.05 nN. We also evaluated two triazole handles when pulling from the alkyne moiety, intriguingly, handle **56** shows a lower value in both k_{eff} and

https://doi.org/10.1021/jacs.4c10346

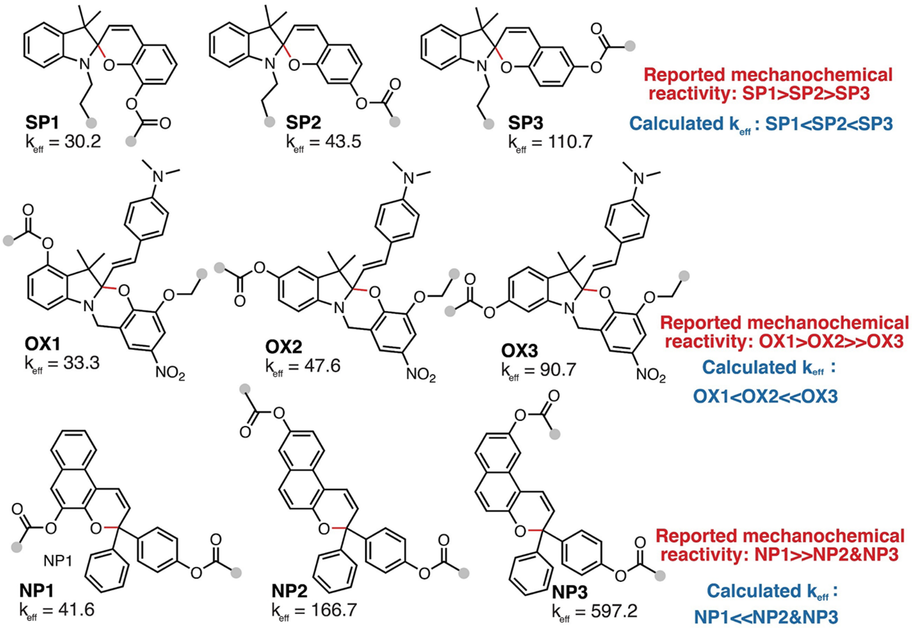

Figure 11. Calculated k_{eff} values (nN Å^{-1}) of the scissile C−O bond in various reported regioisomers of spiropyran (SP), oxazine (OX), and naphthopyran mechanophores. The gray circle represents the atoms to which the force is applied.

Δ*E* compared to **57**. The significantly lowered Δ*E* in **56** is attributed to the better electron delocalization that stabilizes the developing radical species as bond cleavage ensues. Further π-extended naphthalene handles (**58**) were also examined. Regioisomers **58-c** and **58-d** both exhibit exceptionally low k_{eff} values and similar Δ*E* values when compared to benzene hanldes, leading a $f^*_{\mathrm{predicted}}$ below 1.0 nN.

To help visualize the performance of all these handles, the MAX was plotted as shown in Figure 10b. We chose a Δ*E* value of 30.0 kcal mol^{-1} ($t_{1/2}$ > 9 h at 100 °C according to the Erying equation) and a k_{eff} value of 12.0 nN Å^{-1} to further partition the MAX, shown as two dashed lines in Figure 10b. Handles that are located in the top left region are set to be the privileged handles, showing superior mechanochemical couplings but high enough intrinsic bond dissociation energies to be thermally stable. We foresee Figure 10b could provide invaluable guidance on future mechanophore designs and the fine-tuning of their reactivity.

While the discussions so far with RFT and MAX have been mostly focused on C−C bond homolytic cleavages, we believe the principles are likely to be generally adaptable to other bond cleavage mechanisms. We chose three different mechanophores spiropyran (SP),[71] oxazine (OX),[72] and naphthopyran (NP) as the testing examples (Figure 11),[73] which involve C−O bond heterolytic cleavage as the key mechanochemical reaction. We focused on three regioisomers with reported mechanochemical reactivity trend in each class of mechanophores. Here we only calculated the k_{eff} values of the scissile C−O bond, as the Δ*E* values are presumably similar across various regioisomers as suggested in Figure 10a. The calculated k_{eff} values agreed well with the reported reactivity trend qualitatively. For regioisomers that are known to be mechanically inactive (i.e., **OX3**, **NP 2**, and **NP 3**), we observed extremely large k_{eff} values over 90 nN Å^{-1}, implying poor mechanochemical couplings. Notably, in **NP3** we barely observed any C−O elongations with the increase of external force from 1.5 to 2.5 nN, suggesting minimum effective tensile force transmission (Figure S47).

■ CONCLUSION

In this article, we introduced the restoring force triangle (RFT) as a mnemonic device to elucidate the mechanochemical behavior of mechanophores, mostly focusing on C−C bond activations (Figure 1). The RFT is conceptualized from basic models to a sophisticated classification tool. We began with the simplified Hookean spring model (Figure 2) and explored various force profiles (Figure 3), ultimately leading to the RFT inspired by the compound bow's restoring force curve (Figure 4). The Morse potential and its corresponding restoring force curve (Figure 6) provided a way to parametrize the RFT, demonstrating how Δ*E* and k_{eff} can be computed. Importantly, k_{eff} embodies attributes of force transmission to the scissile bond, including geometric (e.g., lever arm effects), stereochemical, and electronic features. The emergence of new states upon mechanical activation (Figure 5) and the segmentation of energy contributions to bond scission (Figure 7) further highlighted the practical applications of the RFT.

Importantly, through a series of comparative analyses and visualizations, we demonstrated how the RFT's key parameters, Δ*E* and k_{eff}, provide a clear distinction between thermal and mechanical contributions to reactivity. This separation fundamentally redefines our approach to mechanophore invention, enabling us to predict and enhance mechanical activation without compromising thermal stability.

The RFT and these foundational models enable us to visualize mechanochemical activity through comparative analyses (Figure 8). The mechanophore activity matrix (MAX) (Figure 9) offered a powerful classification tool, organizing known mechanophores into a framework that reveals critical patterns and insights. We also employed the MAX to evaluate over 40 linker structures to identify the privileged handles (Figure 10). Finally, we went beyond C−C bonds and used k_{eff} values to examine the mechanochemical reactivities of C−O bonds in various regioisomers (Figure 11).

In conclusion, the RFT and the mechanophore activity matrix provide a robust framework for understanding and designing mechanophores. By partitioning thermal stability and mechanical reactivity, this approach offers a new lens through which to view mechanochemistry, paving the way for innovative applications and advancements in the field.

■ ASSOCIATED CONTENT

Supporting Information

The Supporting Information is available free of charge at https://pubs.acs.org/doi/10.1021/jacs.4c10346.

> All simulation and derivation details; the interactive python tool to construct RFT and k_{eff} calculations; methods; overstretching Hookean spring; numerical derivations on RFT; interactive visualization tool on constructing RFT; effective spring constant k_{eff} calculations of various handles; effective spring constant k_{eff} calculations of C–O bond in regioisomers (PDF)

■ AUTHOR INFORMATION

Corresponding Author

Jeffrey S. Moore − *Department of Chemistry, University of Illinois Urbana−Champaign, Urbana, Illinois 61801, United States; Beckman Institute for Advanced Science and Technology, University of Illinois Urbana−Champaign, Urbana, Illinois 61801, United States;* orcid.org/0000-0001-5841-6269; Email: jsmoore@illinois.edu

Authors

Yunyan Sun − *Department of Chemistry, University of Illinois Urbana−Champaign, Urbana, Illinois 61801, United States; Beckman Institute for Advanced Science and Technology, University of Illinois Urbana−Champaign, Urbana, Illinois 61801, United States;* orcid.org/0000-0002-6846-531X

Fangbai Xie − *Department of Chemistry, University of Illinois Urbana−Champaign, Urbana, Illinois 61801, United States; Beckman Institute for Advanced Science and Technology, University of Illinois Urbana−Champaign, Urbana, Illinois 61801, United States;* orcid.org/0009-0003-8307-7969

Complete contact information is available at: https://pubs.acs.org/10.1021/jacs.4c10346

Notes

The authors declare no competing financial interest.

■ ACKNOWLEDGMENTS

We thank Dorothy Loudermilk for figure designs. This work was supported by the NSF Center for the Chemistry of Molecularly Optimized Networks (MONET), CHE-2116298.

■ REFERENCES

(1) Li, J.; Nagamani, C.; Moore, J. S. Polymer Mechanochemistry: From Destructive to Productive. *Acc. Chem. Res.* **2015**, *48*, 2181−2190.

(2) De Bo, G. Polymer Mechanochemistry and the Emergence of the Mechanophore Concept. *Macromolecules* **2020**, *53*, 7615−7617.

(3) Chen, Y.; Mellot, G.; Van Luijk, D.; Creton, C.; Sijbesma, R. P. Mechanochemical Tools for Polymer Materials. *Chem. Soc. Rev.* **2021**, *50*, 4100−4140.

(4) Beyer, M. K.; Clausen-Schaumann, H. Mechanochemistry: The Mechanical Activation of Covalent Bonds. *Chem. Rev.* **2005**, *105*, 2921−2948.

(5) Ribas-Arino, J.; Marx, D. Covalent Mechanochemistry: Theoretical Concepts and Computational Tools with Applications to Molecular Nanomechanics. *Chem. Rev.* **2012**, *112*, 5412−5487.

(6) Caruso, M. M.; Davis, D. A.; Shen, Q.; Odom, S. A.; Sottos, N. R.; White, S. R.; Moore, J. S. Mechanically-Induced Chemical Changes in Polymeric Materials. *Chem. Rev.* **2009**, *109*, 5755−5798.

(7) Davis, D. A.; Hamilton, A.; Yang, J.; Cremar, L. D.; Van Gough, D.; Potisek, S. L.; Ong, M. T.; Braun, P. V.; Martínez, T. J.; White, S. R.; et al. Force-Induced Activation of Covalent Bonds in Mechanoresponsive Polymeric Materials. *Nature* **2009**, *459*, 68−72.

(8) Berkowski, K. L.; Potisek, S. L.; Hickenboth, C. R.; Moore, J. S. Ultrasound-Induced Site-Specific Cleavage of Azo-Functionalized Poly(Ethylene Glycol). *Macromolecules* **2005**, *38*, 8975−8978.

(9) Ong, M. T.; Leiding, J.; Tao, H.; Virshup, A. M.; Martínez, T. J. First Principles Dynamics and Minimum Energy Pathways for Mechanochemical Ring Opening of Cyclobutene. *J. Am. Chem. Soc.* **2009**, *131*, 6377−6379.

(10) Ribas-Arino, J.; Shiga, M.; Marx, D. Understanding Covalent Mechanochemistry. *Angew. Chem., Int. Ed.* **2009**, *48*, 4190−4193.

(11) De Boer, J. H. The Influence of van Der Waals' Forces and Primary Bonds on Binding Energy, Strength and Orientation, with Special Reference to Some Artificial Resins. *Trans. Faraday Soc.* **1936**, *32*, 10−37.

(12) Kauzman, W.; Eyring, H. The Viscous Flow of Large Molecules. *J. Am. Chem. Soc*, **1940**, *62*, pp. 3113−3125.

(13) Bell, G. I. Models for the Specific Adhesion of Cells to Cells. *Science* **1978**, *200*, 618−627.

(14) Evans, E.; Ritchie, K. Dynamic Strength of Molecular Adhesion Bonds. *Biophys. J.* **1997**, *72*, 1541−1555.

(15) Stauch, T.; Dreuw, A. Advances in Quantum Mechanochemistry: Electronic Structure Methods and Force Analysis. *Chem. Rev.* **2016**, *116*, 14137−14180.

(16) Odell, J. A.; Muller, A. J.; Narh, K. A.; Keller, A. Degradation of Polymer Solutions in Extensional Flows. *Macromolecules* **1990**, *23*, 3092−3103.

(17) Beyer, M. K. The Mechanical Strength of a Covalent Bond Calculated by Density Functional Theory. *J. Chem. Phys.* **2000**, *112*, 7307−7312.

(18) Konda, S. S. M.; Brantley, J. N.; Bielawski, C. W.; Makarov, D. E. Chemical Reactions Modulated by Mechanical Stress: Extended Bell Theory. *J. Chem. Phys.* **2011**, *135* (16), 164103.

(19) Wang, S.; Panyukov, S.; Rubinstein, M.; Craig, S. L. Quantitative Adjustment to the Molecular Energy Parameter in the Lake-Thomas Theory of Polymer Fracture Energy. *Macromolecules* **2019**, *52*, 2772−2777.

(20) Chung, C. M.; Roh, Y. S.; Cho, S. Y.; Kim, J. G. Crack Healing in Polymeric Materials via Photochemical [2 + 2] Cycloaddition. *Chem. Mater.* **2004**, *16*, 3982−3984.

(21) Hickenboth, C. R.; Moore, J. S.; White, S. R.; Sottos, N. R.; Baudry, J.; Wilson, S. R. Biasing Reaction Pathways with Mechanical Force. *Nature* **2007**, *446*, 423−427.

(22) Kryger, M. J.; Munaretto, A. M.; Moore, J. S. Structure-Mechanochemical Activity Relationships for Cyclobutane Mechanophores. *J. Am. Chem. Soc.* **2011**, *133*, 18992−18998.

(23) Liu, Y.; Holm, S.; Meisner, J.; Jia, Y.; Wu, Q.; Woods, T. J.; Martinez, T. J.; Moore, J. S. Flyby Reaction Trajectories: Chemical Dynamics under Extrinsic Force. *Science* **2021**, *373*, 208−212.

(24) Diesendruck, C. E.; Steinberg, B. D.; Sugai, N.; Silberstein, M. N.; Sottos, N. R.; White, S. R.; Braun, P. V.; Moore, J. S. Proton-Coupled Mechanochemical Transduction: A Mechanogenerated Acid. *J. Am. Chem. Soc.* **2012**, *134*, 12446−12449.

(25) Sun, Y.; Neary, W. J.; Huang, X.; Kouznetsova, T. B.; Ouchi, T.; Kevlishvili, I.; Wang, K.; Chen, Y.; Kulik, H. J.; Craig, S. L.; et al. A Thermally Stable SO2-Releasing Mechanophore: Facile Activation, Single-Event Spectroscopy, and Molecular Dynamic Simulations. *J. Am. Chem. Soc.* **2024**, *146*, 10943−10952.

(26) Sun, Y.; Neary, W. J.; Burke, Z. P.; Qian, H.; Zhu, L.; Moore, J. S. Mechanically Triggered Carbon Monoxide Release with Turn-On Aggregation-Induced Emission. *J. Am. Chem. Soc.* **2022**, *144*, 1125−1129.

(27) Chen, Z.; Mercer, J. A. M.; Zhu, X.; Romaniuk, J. A. H.; Pfattner, R.; Cegelski, L.; Martinez, T. J.; Burns, N. Z.; Xia, Y.

Mechanochemical Unzipping of Insulating Polyladderene to Semiconducting Polyacetylene. *Science* **2017**, *357*, 475−479.

(28) Horst, M.; Meisner, J.; Yang, J.; Kouznetsova, T. B.; Craig, S. L.; Martínez, T. J.; Xia, Y. Mechanochemistry of Pterodactylane. *J. Am. Chem. Soc.* **2024**, *146*, 884−891.

(29) Horst, M.; Yang, J.; Meisner, J.; Kouznetsova, T. B.; Martínez, T. J.; Craig, S. L.; Xia, Y. Understanding the Mechanochemistry of Ladder-Type Cyclobutane Mechanophores by Single Molecule Force Spectroscopy. *J. Am. Chem. Soc.* **2021**, *143*, 12328−12334.

(30) Nixon, R.; De Bo, G. Three Concomitant C−C Dissociation Pathways during the Mechanical Activation of an N-Heterocyclic Carbene Precursor. *Nat. Chem.* **2020**, *12*, 826−831.

(31) Chen, Y.; Spiering, A. J. H.; Karthikeyan, S.; Peters, G. W. M.; Meijer, E. W.; Sijbesma, R. P. Mechanically Induced Chemiluminescence from Polymers Incorporating a 1,2-Dioxetane Unit in the Main Chain. *Nat. Chem.* **2012**, *4*, 559−562.

(32) Larsen, M. B.; Boydston, A. J. Flex-Activated" Mechanophores: Using Polymer Mechanochemistry to Direct Bond Bending Activation. *J. Am. Chem. Soc.* **2013**, *135*, 8189−8192.

(33) Wang, L.; Zheng, X.; Kouznetsova, T. B.; Yen, T.; Ouchi, T.; Brown, C. L.; Craig, S. L. Mechanochemistry of Cubane. *J. Am. Chem. Soc.* **2022**, *144*, 22865−22869.

(34) Ding, S.; Wang, W.; Germann, A.; Wei, Y.; Du, T.; Meisner, J.; Zhu, R.; Liu, Y. Bicyclo[2.2.0]Hexene: A Multicyclic Mechanophore with Reactivity Diversified by External Forces. *J. Am. Chem. Soc.* **2024**, *146*, 6104−6113.

(35) Suwada, K.; Ieong, A. W.; Lo, H. L. H.; De Bo, G. Furan Release via Force-Promoted Retro-[4 + 2][3 + 2] Cycloaddition. *J. Am. Chem. Soc.* **2023**, *145*, 20782−20785.

(36) Jung, S.; Yoon, H. J. Mechanical Force Induces Ylide-Free Cycloaddition of Nonscissible Aziridines. *Angew. Chem., Int. Ed.* **2020**, *59*, 4883−4887.

(37) Barbee, M. H.; Wang, J.; Kouznetsova, T.; Lu, M.; Craig, S. L. Mechanochemical Ring-Opening of Allylic Epoxides. *Macromolecules* **2019**, *52*, 6234−6240.

(38) Lin, Y.; Kouznetsova, T. B.; Craig, S. L. A Latent Mechanoacid for Time-Stamped Mechanochromism and Chemical Signaling in Polymeric Materials. *J. Am. Chem. Soc.* **2020**, *142*, 99−103.

(39) Lenhardt, J. M.; Black, A. L.; Craig, S. L. Gem-Dichlorocyclopropanes as Abundant and Efficient Mechanophores in Polybutadiene Copolymers under Mechanical Stress. *J. Am. Chem. Soc.* **2009**, *131*, 10818−10819.

(40) Kean, Z. S.; Niu, Z.; Hewage, G. B.; Rheingold, A. L.; Craig, S. L. Stress-Responsive Polymers Containing Cyclobutane Core Mechanophores: Reactivity and Mechanistic Insights. *J. Am. Chem. Soc.* **2013**, *135*, 13598−13604.

(41) Klukovich, H. M.; Kouznetsova, T. B.; Kean, Z. S.; Lenhardt, J. M.; Craig, S. L. A Backbone-Arm Effect Enhances Polymer Mechanochemistry. *Nat. Chem.* **2013**, *5*, 110−114.

(42) Lenhardt, J. M.; Ong, M. T.; Choe, R.; Evenhuis, C. R.; Martinez, T. J.; Craig, S. L. Trapping a Diradical Transition State by Mechanochemical Polymer Extension. *Science* **2010**, *329*, 1057−1060.

(43) Wang, J.; Kouznetsova, T. B.; Niu, Z.; Ong, M. T.; Klukovich, H. M.; Rheingold, A. L.; Martinez, T. J.; Craig, S. L. Inducing and Quantifying Forbidden Reactivity with Single-Molecule Polymer Mechanochemistry. *Nat. Chem.* **2015**, *7*, 323−327.

(44) Wang, S.; Hu, Y.; Kouznetsova, T. B.; Sapir, L.; Chen, D.; Herzog-Arbeitman, A.; Johnson, J. A.; Rubinstein, M.; Craig, S. L. Facile Mechanochemical Cycloreversion of Polymer Cross-Linkers Enhances Tear Resistance. *Science* **2023**, *380*, 1248−1252.

(45) Wang, Z.; Zheng, X.; Ouchi, T.; Kouznetsova, T. B.; Beech, H. K.; Av-Ron, S.; Matsuda, T.; Bowser, B. H.; Wang, S.; Johnson, J. A.; et al. Toughening Hydrogels through Force-Triggered Chemical Reactions That Lengthen Polymer Strands. *Science* **2021**, *374*, 193−196.

(46) Imato, K.; Irie, A.; Kosuge, T.; Ohishi, T.; Nishihara, M.; Takahara, A.; Otsuka, H. Mechanophores with a Reversible Radical System and Freezing-Induced Mechanochemistry in Polymer Solutions and Gels. *Angew. Chem., Int. Ed.* **2015**, *54*, 6168−6172.

(47) Zhang, H.; Li, X.; Lin, Y.; Gao, F.; Tang, Z.; Su, P.; Zhang, W.; Xu, Y.; Weng, W.; Boulatov, R. Multi-Modal Mechanophores Based on Cinnamate Dimers. *Nat. Commun.* **2017**, *8* (1), 1147.

(48) Yang, J.; Horst, M.; Werby, S. H.; Cegelski, L.; Burns, N. Z.; Xia, Y. Bicyclohexene-Peri-Naphthalenes: Scalable Synthesis, Diverse Functionalization, Efficient Polymerization, and Facile Mechanoactivation of Their Polymers. *J. Am. Chem. Soc.* **2020**, *142*, 14619−14626.

(49) Yang, J.; Horst, M.; Romaniuk, J. A. H.; Jin, Z.; Cegelski, L.; Xia, Y. Benzoladderene Mechanophores: Synthesis, Polymerization, and Mechanochemical Transformation. *J. Am. Chem. Soc.* **2019**, *141*, 6479−6483.

(50) Hu, Y.; Wang, L.; Kevlishvili, I.; Wang, S.; Chiou, C. Y.; Shieh, P.; Lin, Y.; Kulik, H. J.; Johnson, J. A.; Craig, S. L. Self-Amplified HF Release and Polymer Deconstruction Cascades Triggered by Mechanical Force. *J. Am. Chem. Soc.* **2024**, *146*, 10115−10123.

(51) Chen, Z.; Zhu, X.; Yang, J.; Mercer, J. A. M.; Burns, N. Z.; Martinez, T. J.; Xia, Y. The Cascade Unzipping of Ladderane Reveals Dynamic Effects in Mechanochemistry. *Nat. Chem.* **2020**, *12*, 302−309.

(52) Hibbeler, R. C. *Engineering Mechanics: statics*, 12 th ed.; Pearson Prentice Hall, 2010.

(53) Laidler, K. J.; King, M. C. The Development of Transition-State Theory. *J. Phys. Chem.* **1983**, *87*, 2657−2664.

(54) In contrast to TST, non-statistical molecular dynamics (NSMD) takes into account the time-dependent behavior of reacting molecules. NSMD simulations utilize computational techniques to model and simulate the motion and interactions of atoms and molecules during a chemical reaction. NSMD can also take into consideration external forces if they are present. A detailed discussion about these topics was covered elsewhere and will not be the focus of this paper.

(55) Hass, C. *How compound bow works*. https://www.outsideonline.com/outdoor-gear/tools/how-compound-bows-work/. 2017. accessed 2024-July-11.

(56) Tiermas, M. An Advanced Model of the Round-Wheel Compound Bow. *Meccanica* **2016**, *51*, 1201−1207.

(57) Morse, P. M. Diatomic Molecules According to the Wave Mechanics. II. Vibrational Levels. *Phys. Rev.* **1929**, *34*, 57.

(58) Müser, M. H.; Sukhomlinov, S. V.; Pastewka, L. Interatomic Potentials: Achievements and Challenges. *Adv. Phys.: x* **2023**, *8*, 2093129.

(59) Sun, Y.; Kevlishvili, I.; Kouznetsova, T. B.; Burke, Z. P.; Craig, S. L.; Kulik, H. J.; Moore, J. S. The Tension Activated Carbon-Carbon Bond. *Chem* **2024**, *10*, 3055−3066.

(60) Stevenson, R.; De Bo, G. Controlling Reactivity by Geometry in Retro-Diels-Alder Reactions under Tension. *J. Am. Chem. Soc.* **2017**, *139*, 16768−16771.

(61) Wang, J.; Kouznetsova, T. B.; Kean, Z. S.; Fan, L.; Mar, B. D.; Martínez, T. J.; Craig, S. L. A Remote Stereochemical Lever Arm Effect in Polymer Mechanochemistry. *J. Am. Chem. Soc.* **2014**, *136*, 15162−15165.

(62) Flear, E. J.; Horst, M.; Yang, J.; Xia, Y. Force Transduction Through Distant Force-Bearing Regioisomeric Linkages Affects the Mechanochemical Reactivity of Cyclobutane. *Angew. Chem. Int. Ed.* **2024**, *63* (33), No. e202406103.

(63) Barbee, M. H.; Kouznetsova, T.; Barrett, S. L.; Gossweiler, G. R.; Lin, Y.; Rastogi, S. K.; Brittain, W. J.; Craig, S. L. Substituent Effects and Mechanism in a Mechanochemical Reaction. *J. Am. Chem. Soc.* **2018**, *140*, 12746−12750.

(64) Brown, C. L.; Bowser, B. H.; Meisner, J.; Kouznetsova, T. B.; Seritan, S.; Martinez, T. J.; Craig, S. L. Substituent Effects in Mechanochemical Allowed and Forbidden Cyclobutene Ring-Opening Reactions. *J. Am. Chem. Soc.* **2021**, *143*, 3846−3855.

(65) Hammond, G. S. A Correlation of Reaction Rates. *J. Am. Chem. Soc.* **1955**, *77* (2), 334−338.

(66) Bowser, B. H.; Wang, S.; Kouznetsova, T. B.; Beech, H. K.; Olsen, B. D.; Rubinstein, M.; Craig, S. L. Single-Event Spectroscopy and Unravelling Kinetics of Covalent Domains Based on Cyclobutane Mechanophores. *J. Am. Chem. Soc.* **2021**, *143*, 5269−5276.

(67) Neary, W. J.; Sun, Y.; Moore, J. S. Selective Ring-Opening Allene Metathesis: Polymerization or Ruthenium Vinylidene Formation. *ACS Macro Lett.* **2021**, *10*, 642−648.

(68) Neary, W. J.; Zhao, F.; Murphy, M. C.; Chen, Y.; Liu, F.; Houk, K. N.; Moore, J. S. Substituent Effects on Ring Opening Allene Metathesis: Polymerization Rate Enhancement and Regioregularity. *Macromolecules* **2024**, *57*, 5350−5357.

(69) Moses, J. E.; Moorhouse, A. D. The Growing Applications of Click Chemistry. *Chem. Soc. Rev.* **2007**, *36*, 1249−1262.

(70) Jin, Y.; Yu, C.; Denman, R. J.; Zhang, W. Recent Advances in Dynamic Covalent Chemistry. *Chem. Soc. Rev.* **2013**, *42*, 6634−6654.

(71) Lin, Y.; Barbee, M. H.; Chang, C. C.; Craig, S. L. Regiochemical Effects on Mechanophore Activation in Bulk Materials. *J. Am. Chem. Soc.* **2018**, *140*, 15969−15975.

(72) Qian, H.; Purwanto, N. S.; Ivanoff, D. G.; Halmes, A. J.; Sottos, N. R.; Moore, J. S. Fast Reversible Mechanochromism of Regioisomeric Oxazine Mechanophores: Developing in Situ Responsive Force Probes for Polymeric Materials. *Chem.* **2021**, *7*, 1080−1091.

(73) Robb, M. J.; Kim, T. A.; Halmes, A. J.; White, S. R.; Sottos, N. R.; Moore, J. S. Regioisomer-Specific Mechanochromism of Naphthopyran in Polymeric Materials. *J. Am. Chem. Soc.* **2016**, *138*, 12328−12331.

https://doi.org/10.1021/jacs.4c10346